Toward Monitoring The Relationship Between Vegetation Conditions And Volcanic Activity With HyspIRI

Summary of Research

NASA Award Number: NNX11AE45G

Performance period: 2/1/2011 -12/31/2012

Submitted by

Principal Investigator:

Alexander Koltunov

Center for Spatial Technologies and Remote Sensing (CSTARS)
University of California, Davis
121 Veihmeyer Hall, One Shields Avenue, Davis, CA 95616
ph. (530) 752-5092

akoltunov@ucdavis.edu

Summary

Toward the project objectives, we have created a 29-date 161-band HyspIRI-like hyperspectral dataset based on Hyperion images in VSWIR over the eastern side of the Island of Hawaii at 60-m spatial resolution between 2005-01-17 and 2010-12-30. In the following, this dataset is referred to as *HyspIRI-161* dataset. This unique dataset included both pre-eruption and post-eruption periods for the recently opened (March 2008) vent at Kilauea volcano's Halemaumau pit crater, Hawaii. This image sequence was atmospherically corrected, co-registered to subpixel accuracy, and used to produce auxiliary derived products: clouds/shadow masks, and 25 conventional vegetation indexes.

Furthermore, we developed *iProsail*, a Matlab-based toolbox for computationally efficient inversion of PROSAILH radiative transfer model (*aka*. PROSAIL-5B), which couples PROSPECT-5 and 4SAIL (Verhoef 2007). Our toolbox is based on numerical techniques for constrained non-linear optimization available in Matlab. We applied *iProsail* to 128-band spectra of HyspIRI-161 images and calculated spatially explicit measurements of vegetation biophysical/biochemical properties and extent on an unprecedentedly massive spatial and temporal scales. Using these retrievals we gained a better understanding of the issues and sources of uncertainties and biases in the retrieved biochemistry and structure over satellite image time series. In particular, we found that PROSAILH inversion results are very sensitive to the sun-view geometry, and soil spectrum brightness. We also determined that HyspIRI spectral resolution is sufficiently high to maintain high accuracy of computationally efficient inversion approaches.

Furthermore, using a subset of the HyspIRI-like images time series we also illustrated over a selected regions that HyspIRI will be able to detect and map changes in vegetation properties near the volcano, which may be caused by volcanic activity. A conclusion about the cause-effect relationship between changes in the remotely estimated vegetation properties and the degassing is beyond the scope of our research. However, we have provided the evidence that HyspIRI, with its high frequency and spectral resolution and coverage, will help generate useful spatially explicit hypotheses for subsequent multi-disciplinary studies of the relationship between vegetation and volcanoes.

1. Introduction

The central Objective of this project is to

> *Demonstrate that vegetation-volcano relationship will be observable by the future HyspIRI mission*

We are focusing on investigating the potential impacts of the recently opened (March 2008) vent at Kilauea volcano's Halemaumau pit crater, Hawaii, on the vegetation surrounding the volcano. During 2008-2009 this vent emitted large amounts of gasses in the atmosphere, with potential impacts on the vegetation in proximity to the volcano.

Out work was planned to advance in three stages aimed at the following sub-goals:

- I.a. Characterize biophysical/biochemical and structural properties of the vegetation on the eastern side of the Big Island;
- I.b. Determine the average spatial pattern of SO_2 distribution, based on the state-of-the-art high-resolution models for concentration and dispersion of volcanic gas and aerosol
- I.c. Determine evidence of dependence/correlation/co-occurrence that exists between vegetation type and stress and the average SO_2 distribution pattern.

2. Research Activities

2.1. Study area and HyspIRI-161 image sequence

The study was conducted over the Eastern Island of Hawaii based on the data from recent Hyperion acquisitions (Figure A1). Although we preliminarily identified ~150 swaths of Hyperion data collected during Jan 2005 to Dec 2010 over the eastern and south-eastern part of the Island, many of the images from Hyperion that we planned to include in the analysis, were unsuitable due to high cloud cover or difference in the smile effect bias between different flightlines. We selected 29 hyperspectral images with low-to moderate cloud cover that cover dry and wet seasons and both periods: before the new vent opened (Jan 2005 –Feb 2008) and after the vent opened (March 2008 – Dec 2010). Figure A2 illustrates the temporal coverage of the HyspIRI-161 image sequence. Hyperion does not have thermal bands, and we planned to augment Hyperion with a few non-cloudy ASTER scenes nearly-co-occurring with Hyperion overflights. However, we were unable to do so due to the extensive effort to compile, preprocess, and analyze the multi-temporal hyperspectral data of HyspIRI-161 and not enough time to do a comparable effort on the thermal data.

2.2. Algorithm/software development for PROSAILH inversion over remote sensing images

Full numerical inversion of radiative transfer models (RTM), such as PROSAILH, on massive scales of satellite image sequences has not been ever attempted, to the best of our knowledge. Although orders of magnitude faster than look-up table approach to PROSAILH inversion, the numerical inversion is a computer-intensive procedure, too. Furthermore, there are many factors that influence the quality and computational efficiency of PROSAILH inversion: ranging from purely technical (e.g. accounting for missing values for some bands for some pixels, variations in input data format, or memory management), to more delicate (e.g. choosing error functional to be minimized, initial values and constraints for some variables, a stopping criterion for the iterative process, etc.).

We have developed a *Matlab*-based software toolbox, called *iProsail*, for PROSAILH numerical inversion by constrained non-linear least squares optimization and tested iProsail for use with Hyperion, AVIRIS, and MASTER remote sensing images. The software toolbox is functional now and reasonably stable. This toolbox is based on the PROSPECT-5 and 4SAIL forward Matlab code publicly available at http://teledetection.ipgp.jussieu.fr/prosail/. We have also incorporated a recent updated code of PROSAILH from Dr. J-B Feret with improvements of leaf inclination distribution function (LIDF) estimation. This code implements a finer scale tabulation of the average leaf inclination angle (ALA) for high angles (closer to 90°), under the elliptical model of LIDF.

In this report, we present PROSAILH inversion with respect to the following parameters:

- leaf structure parameter,
- chlorophyll a+b content,
- carotenoids content,
- brown pigments content,
- equivalent water thickness,
- dry matter content,
- average leaf angle (under elliptical LIDF model),
- leaf area index,
- hot spot coefficient.

Below in this document, the vector of parameter is generically referred to as θ. Other parameters of the PROSAILH model were assumed known fixed constants (e.g. sun-view angles or diffused radiation fraction). Table 1 provides complete information about parameters and the constrained numerical inversion options used to invert PROSAILH with respect to θ. Furthermore, 33 of 161 bands (430 to 460 nm and 1990 to 2320 nm) of HyspIRI-161 were not used for PROSAILH inversion to very low signal-to-noise ratios. Thus, the inversion used only 128 bands of HyspIRI-161.

2.2.1. Computational aspects: HyspIRI spectral resolution is sufficiently high to enable computationally economical numerical inversion modes.

Numerical inversion of PROSAILH is an iterative process that starts with the input spectrum $\rho(\lambda_s)$ and initial parameters vector θ_0. At each iteration a numerical inversion algorithm runs PROSAILH in a forward mode a number of times to improve the value of θ. In every run, PROSAILH uses a set of pre-determined specific absorption coefficient spectra $\tau(\lambda)$ of biochemical constituents (pigments , water, and dry matter, see Figure D) to model a reflectance spectrum $\rho_m(\lambda, \theta)$. This spectrum needs to be convolved with the sensor response function and resampled, resulting in a sensor-like modeled spectrum $\rho_m(\lambda_s, \theta)$ which can be compared with $\rho(\lambda_s)$. In a standard approach, for each biochemical $\tau(\lambda)$ is a 2100-element vector (λ being sampled at 1nm step) and so is the resulting $\rho_m(\lambda, \theta)$, leading to considerable computational challenges due to hundreds-to-thousands of iterations typically needed for inversion. Future operational inversion of PROSAILH over HyspIRI images, necessitates improvement in the inversion techniques, without significantly reducing the inversion accuracy.

To improve efficiency, we suggest modifying the inversion approach as follows: we smoothed and resampled $\tau(\lambda)$ *once* and used the sensor-like $\tau(\lambda_s)$ in PROSAILH, thereby generating $\rho_m(\lambda_s, \theta)$ *directly*. In other words, we run PROSAILH at the HyspIRI spectral resolution, bypassing generation of auxiliary 1-nm resolution spectra. This produces a nearly order of magnitude reduction in processing time. Does the proposed modification lead to significantly different inversion results? Our experiment with HyspIRI-161 image time series indicates that the largest difference was observed in Chl-ab estimation, with relative error varying between 3-6% for different dates (see Figure E1, for example). For other parameters the differences are an order of magnitude smaller and thus the results are virtually identical.

Importantly, for sensors at low spectral resolution (such as MASTER) , the inversion using MASTER-like absorption spectra results in large spectrum modeling residuals, especially in VIS range (Figure E2) , and large biases for most of the retrieved parameters (Figure E3).

2.2.2. Choice of soil spectrum

By running PROSAILH inversion with the input soil spectra scaled by different scale factors (Figure F1), we observed that brightness of background soil spectrum for PROSAILH inversion critically influences estimates of θ. Figure F2 illustrates this point by the example of brown pigment concentration (C_{brown}). Other interesting correlations between soil brightness and θ that we consistently observed in our experiments are summarized in Table 2.

2.3. Data processing and compiling HyspIRI-161 image sequence and ancillary datasets

2.3.1. Image co-registration across time

To construct a HyspIRI-like image sequence we used L1GsT ortho-corrected and geo-referenced Hyperion images. Unfortunately, these georeferenced images often suffer from residual misalignment by up to hundreds of meters (or several pixels), introducing additional complexities to subsequent multi-temporal analyses. Therefore, we additionally co-registered the Hyperion images using an automated image registration technique (Koltunov et al. 2012) that combines robust band-wise compensation for radiometric differences in images (Koltunov et al. 2008) with an iterative gradient-based video-sequence alignment method by Irani (2002), under the affine image motion model. As a result of the image co-registration, the residual pixel misregistration was markedly reduced to sub-pixel level (estimated range of residual displacement 0-0.3 pixels) allowing more accurate analysis of the changes in vegetation conditions.

2.3.2. Atmospheric Correction

The Hyperion image sequence was atmospherically corrected with ATCOR software with the following options: tropical atmosphere class, water vapor =3-5 gr/cm^2; Visibility = 80 km; rural aerosol model. Figure B shows examples of averaged vegetation spectra after correction. As can be seen in Figure B, the corrected spectra exhibit the typical absorption features of leaf pigments in the 400- to 700-nm region and liquid water in the SWIR region (e.g. at 970, 1130, and 1200 nm). Relatively low reflectance values across the spectrum can be attributed to shadowing caused by low sun angle (~40 degrees) and tall, heterogeneous canopies, resulting in substantial shadowing at different spatial scales, and possible residual errors of ATCOR-based correction.

2.3.3. Cloud, plume, and shadow mapping

Each image in the HyspIRI-161 sequence was processed independently for cloud, plume and cloud shadow delineation. We used a supervised classification method, in which the training samples for classes CLEAR, CLOUD, SHADOW, and PLUME were input to a supervised classifier that models each class as a Gaussian Mixture with unrestricted covariance structure of the mixture components and estimates the data distribution parameters using the Expectation-Maximization algorithm (Dempster et al. 1977), with the Bayesian Information Criterion (Schwarz, 1978) used to select the class-conditional mixture models. The Bayes classifier was intentionally biased toward under-classifying clear pixels by accepting class CLEAR only if its posterior probability exceeded 90%. Figure C displays an example of the resulting classification images.

2.3.4. Empirical radiometric normalization of reflectances to compensate for BRDF

Atmospherically corrected reflectance spectra for different images exhibit substantial variability in overall brightness (Figure G1, left). These differences could be attributed to varying sun-view geometry for different images, and also potential biases in atmospheric correction. Using a normalized-difference VI would partly mitigate the impact of this variability on the change analysis. In contrast, PROSAILH attempts to use the input sun-view geometry information to account for BRDF effect on reflectance spectra. Our experiments indicate that unfortunately, PROSAILH did not do this job perfectly with the HyspIRI-161 images, and the resulting retrieved time series of θ(t) were greatly affected by the sun-view geometry. Figure G2 (top row) illustrates this phenomenon in the example of one of the most critical structural parameter, θ_{ALA} (average leaf angle), which is totally unrealistically estimated as ~0° (horizontal leaves and canopies) over large clear-sky image areas.

To further understand and reduce these effects, for each image with the timestamp t_i , we statistically estimated a relative normalization factor $\beta(t_i)$ that radiometrically normalizes the reflectance toward baseline image (chosen to be image #26 with t_{bas}=2010.01.16). Specifically, for each reflectance band at wavelength λ_k, we assumed the model:

$$\beta(t_i)\rho(\lambda_k, t_i) = \rho(\lambda_k, t_{bas})$$

To mitigate the effects of substantial noise inherited from Hyperion, undetected cloud/shadow, and surface changes, we estimated β by a robust regression of the median spectra of ~9,000-13,000 pixels (depending on data availability at t_{bas} and t_i). Only VIS spectral bands were used to calculate $\beta(t_i)$. The obtained values for the coefficients $\beta(t_i)$ are listed in the last column of Table 3. Figure G3 illustrates that images with similar sun-view geometries (e.g. 2005.01.17 and 2007.01.20, or 2005.06.19, 2006.06.07, and 2007.07.06) always have similar values of β (a proxy for relative brightness), whereas for images with dissimilar geometries this is generally not the case. Figure G2 (bottom row) shows that relative normalization markedly improves inversion (the normalized spectra are shown in Figure G1, right). On the other hand, there is still a residual instability in the θ_{ALA} (Figure G2) and other parameters, esp. θ_{Cab} and θ_{Car} (not shown). This can be explained by the fact that we use a single image-wide empirical correction coefficient, whereas the surface structure generally varies from pixel to pixel. Also, our empirical normalization implicitly over-simplifies the BRDF of the surface to be wavelength-independent. The inversion results presented in this report are obtained with a BRDF-normalized sequence, unless directly stated otherwise.

2.4. Vegetation Change Analysis with HyspIRI-like images and PROSAILH.

2.4.1. Vegetation-volcano relationship analysis

Unfortunately, due to delayed funding on the side of our collaborators from the Univ. of Hawaii, the HYSPLIT model outputs are available only starting from summer 2010 after SO_2 releases from Halemaumau vent dropped significantly, compared to the high volume emissions observed in late 2008 through late 2009. Also, since we were using historic data, we did not have concurrent chemistry data to validate the retrievals from HyspIRI-161 data. Therefore, we used a different approach to assess changes in vegetation cover and conditions that is similar conceptually to the methods used in previous studies (Giglio et al. 2003, Koltunov et al. 2009). Specifically, we investigated whether the dynamics of the vegetation properties in proximity of the Kilauea crater was significantly different than that of a large “baseline” vegetated area that are distant from the volcano. A limitation of this approach is that small-magnitude temporal changes in the inspected region can be masked by changes in the same direction from other causes in the baseline region (type II error) or overemphasized due to the opposite-direction changes in the baseline region (type I error). The advantage of this approach, however, is that it minimizes the temporally variable image-wide biases in vegetation parameter estimation. Some of these biases are caused by varying sun-view geometry and BRDF and were discussed above in sect. 2.X.Y. With large number of pixels for which PROSAILH was inverted, conservative detection of clear-sky pixels, and the use of robust statistics, we estimated the baseline time series for the parameter vector θ(t), which we denote $\theta_b(t)$, as the 20% trimmed mean value over clear-sky and non-shadowed pixels in a baseline ROI (Figure H). The resulting time series for the relative value $\theta_{rel}(s,t)$ at a pixel location *s* is then defined by:

$$\theta_{rel}(s,t) = \theta(s,t) / \theta_b(t).$$

Under the assumption of no disturbance, for any given pixel s, $\theta_{rel}(s,t) = c(s)$, i.e. temporally invariant, and therefore there would be no significant differences between the observed values of $\theta_{rel}(s,t)$.

2.4.2. What HyspIRI-161 + PROSAILH think has happened to vegetation near the volcano

Our experiments have indicated that time series of vegetation biophysical parameters estimated by PROSAILH inversion with HyspIRI-161 spectra allows one to detect vegetation changes and generate useful spatially explicit hypotheses about their nature and possible links with volcanic activity.

To initially assess our estimates of canopy biochemistry and structure, we used information from previous studies in this area (Asner et al. 2006, 2008). These studies used 4 sites representing two dominant overstory species: *Metrosideros Polymorpha* (MP) and *Myrica Faya* (Figure J). According to ground measurements, Metrosideros forests generally lower LAI (3–6) and have lower leaf water content than Myrica (LAI> 5), (Asner et al. 2006, Asner and Vitousek 2005). The arrows in Figure K1 point to the site locations and illustrate that LAI estimated by our PROSAILH inversion correctly represent the LAI differences between these species, however the LAI values are generally underestimated. Similarly, C_w (i.e. the estimates of equivalent water thickness) for Myrica sites is greater than C_w of *M. Polymorpha,* as can be seen in Figure K2.

Furthermore, we consider three ROIs labeled "C", "S", and "D1" that are shown in Figure H. As can be seen in the available high-resolution imagery of these regions (Figure L1), the canopy cover density and possibly biochemical properties of these regions substantially changed between 2002/04/19 and 2010-2011. The PROSAILH inversion with HyspIRI-161 images time series provides additional information about the biochemical features and the dynamics of these changes. Figure L2 shows a zoomed image time series of $\theta_{rel}(s,t)$ for LAI, C_w, C_{brown} and Chl/C_w over these ROIs during wet season. The relative reduction in LAI and C_w, and increase in C_{brown} and Chl/C_w ratio become apparent over the southern parts of these ROIs in the first post-eruption image (2008.12.06) and the damaged area progressively expands northward from that date on.

Some of these changes provide a sufficiently strong signal to influence the average time series of for the entire ROI. Figures MC, MS, and MD1 show their respective average θ time series for LAI C_w, CWC (canopy water), C_{ab}, Car, and C_{brown}. In each Figure, a plot in the left column shows the average θ(t) and $\theta_b(t)$, i.e. the 20% trimmed mean value of for the baseline ROI shown in Figure H. Each plot in the right column shows the corresponding ratio: $\theta_{rel}(s,t)$.

Furthermore, we performed two-sample t-tests of significance for the change in the $\theta_{rel}(s,t)$ between pre-eruption and post-eruption period of the entire ROI as whole. The results presented in Table 4 provide evidence of variable strength for decrease in LAI, CWC (canopy water), and Car, and increase in C_{brown} and C_{ab}. Some of these behaviors are consistent with damage, however, for some of the parameters (such as C_{ab}, Car) we doubt that PROSAILH retrievals were accurate. Alternatively, the apparent significant increase in C_{ab} for remaining plants can be explained by their compensation response to reduction in LAI. Future studies and field data will be needed to resolve this uncertainty.

Spatio-temporal patterns of degradation that are similar to those shown in Figure L2 are also observable in the dry season θ(t) of degradation, however the patterns there are more noisy, we believe due to less accurate relative normalization of post-eruption dry season images with sun-view geometries that are very dissimilar from those of pre-eruption dry season images.

3. Conclusions and Recommendations

In this project, we used PROSAILH (PROSPECT-5 + 4SAIL) radiative transfer model inversion over 128 band image time series from HyspIRI-161 at 60m spatial resolution to characterize vegetation dynamics near the Kilauea crater, the Island of Hawaii. Despite data quality problems, variable cloud cover, dynamic angular effects, and lack of concurrent field data, we were able to detect changes in spatio-temporal patterns both on leaf and canopy level and these changes were consistent with increased vegetation stress for most comparisons. The changes in the LAI retrievals are consistent with the foliage reduction observed in available high resolution images of the area. The ability of PROSAILH and our inversion method to adequately represent gradients of LAI and C_w is indirectly supported by previous field measurements and observations in the study area (Asner & Vitousek, 2005; Asner et al., 2006). In the selected sites, the timing of the first detection of these disturbances (2008.12.06) falls at the beginning of the elevated activity period of the Halemaumau vent. Thus, this work demonstrates an important potential application of HyspIRI data to monitor sub-visual to sub-lethal types of vegetation injury from pollution or other environmental stressors.

Furthermore, this work has advanced our understanding of various aspects of retrieving canopy biochemistry and structure from hyperspectral satellite imagery, especially for multitemporal settings. It is increasingly clear that to accurately retrieve chemistry and structure from reflectance data requires that the scattering properties of a canopy under varying view angles are addressed. We show that major artifacts occur as a consequence of data from differing BRDF and sun-view geometry, at least partly due to changing canopy shadowing and exposure of soil substrate. One way to address variable sun-view geometry would be to plan for HyspIRI BRDF products, such as Nadir-BRDF adjusted reflectance, similar to the corresponding MODIS products. Another important issue is the relationship between computational efficiency and accuracy of operational numerical inversion of PROSAILH. Our experiments indicated that for computational efficiency purposes, during the inversion the PROSAILH can be effectively run at HyspIRI spectral resolution (10 nm) without reduction in accuracy of the retrievals. This appears to be a an interesting subject for future investigation. All in all, we would like to additionally emphasize that we believe that PROSAILH needs significant work before it can be reliably inverted operationally on a time series of HyspIRI data. We suggest that the scientific community needs to invest additional research efforts into improving canopy radiative transfer models and model inversion, to maximize the benefits of HyspIRI from the first days of its operation.

Although with the Hyperion-derived HyspIRI-like image time series we were able to detect relative changes in vegetation cover and conditions near the volcano, we need to have more frequent temporal observations in order to more accurately characterize the timing and dynamics of response to these disturbances and reduce the underlying uncertainties. We look forward to the repeat hyperspectral observations from the future HyspIRI mission.

Acknowledgements

We especially thank Dr. Peter Mouginis-Mark from Univ. of Hawaii for his critical role in the project design. We warmly thank Dr. J-B. Feret (Carnegie Institution) for his great help with the PROSAIL Matlab code and model inversion issues. We appreciate Dr. Mike Griffin (MIT Lincoln Lab) who provided us with A Hyperion Cloud Cover algorithm code that was used for data preprocessing. We also acknowledge helpful communications with Dr. Steven Businger and Mr. Roy Huff on the project onset. We thank Mr. George Scheer (UC Davis) for hardware and system administration and other computational support that enabled us to analyze these data.

References

Asner, G. P., Martin, R. E., Carlson, K. M., Rascher, U., & Vitousek, P. M. (2006). Vegetation–climate interactions among native and invasive species in Hawaiian rainforest. *Ecosystems* 9(7): *1106-1117*.

Asner, G. P., Carlson, K. M., Martin, R. E., (2008) Substrate age and precipitation effects on Hawaiian forest canopies from spaceborne imaging spectroscopy, Remote Sensing of Environment, 98(4): 457–467

Asner G.P., Vitousek P. M. (2005). Remote analysis of biological invasion and biogeochemical change. Proc Nat' Acad Sci USA 102:4383–6.

Cheng, T.**,** Riaño, D., Koltunov, A., Whiting, M. L., Ustin, S. L. & Rodriguez, J. (2013). Detection of diurnal variation in orchard canopy water content using MODIS/ASTER airborne simulator (MASTER) data. *Remote Sensing of Environment*, v.132, pp.1-12.

Dempster, A. P., Laird, N. M., and Rubin, D. B. (1977). Maximum likelihood from incomplete data via the EM-algorithm. *Journal of the Royal Statistical Society, Series B*, 39, 1.38

Giglio, L., Descloitres, J., Justice, C. O., and Kaufman, Y. J., 2003, "An enhanced contextual fire detection algorithm for MODIS". *Remote Sensing of Environment*, v. 87, 273-282, 2003

Irani M (2002). "Multi-Frame Correspondence Estimation Using Subspace Constraints". International Journal of Computer Vision 48: 173-194.

Jacquemoud, S.; Verhoef, W.; Baret, F.; Zarco-Tejada, P.J.; Asner, G.P.; Francois, C.; Ustin, S.L.(2009) " PROSPECT + SAIL models: A review of use for vegetation characterization ", " *Remote Sensing of Environment, ,* v.113 , Supplement 1, Imaging Spectroscopy Special Issue, pp. S56-S66

Koltunov A, Ben-Dor E, Ustin SL (2008) Image construction using multitemporal observations and Dynamic Detection Models. International Journal of Remote Sensing 30: 57-83.

Koltunov, A., Ustin S.L., Asner, G.P., Fung, I., (2009) "Selective logging changes forest phenology in the Brazilian Amazon: Evidence from MODIS images time series analysis", *Remote Sensing of Environment,* v.113 (11) pp. 2431–2440

Koltunov A, Ustin S. L, Quayle B, Schwind B (2012) GOES Early Fire Detection (GOES-EFD) System Prototype. ASPRS 2012 Anuual Conference. Sacramento, CA

Verhoef, W., Xiao, Q., Jia, L., & Su, Z. (2007), Unified optical-thermal four-stream radiative transfer theory for homogeneous vegetation canopies. *IEEE Transactions on Geoscience and Remote Sensing*, *45*, 1808-1822.

Schwarz, G. (1978). Estimation the dimension of a model. *The Annals of Statistics*, 6(2), 461.464.

Figures and Tables

Figure A1: Spatial coverage of Hyperion datasets available for 2005-2010 in the Eastern part of the Island of Hawaii

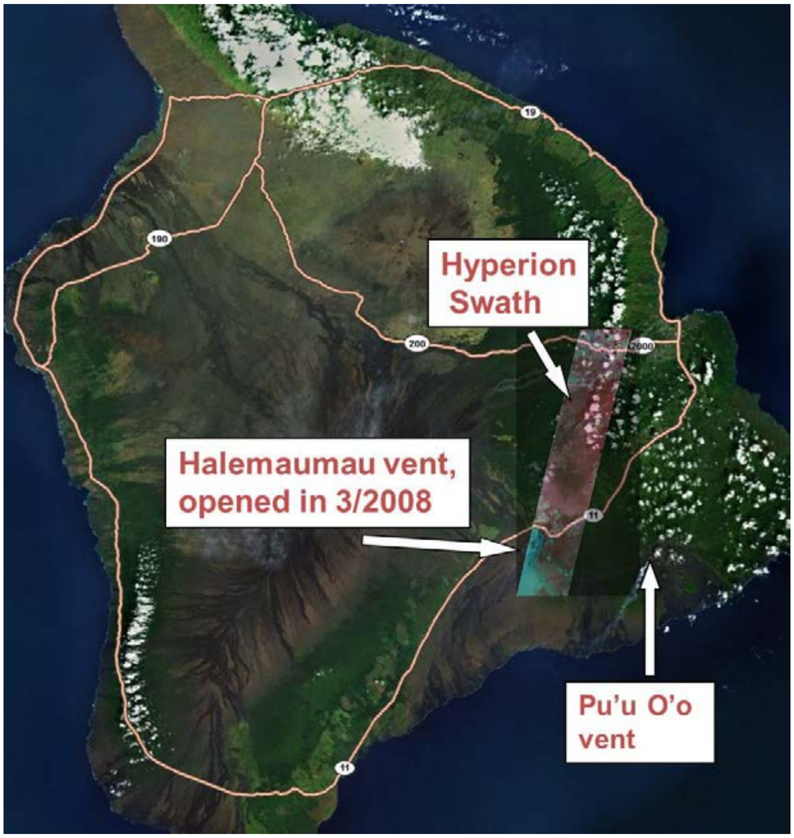

Figure A2: Temporal coverage of the HyspIRI-161 dataset

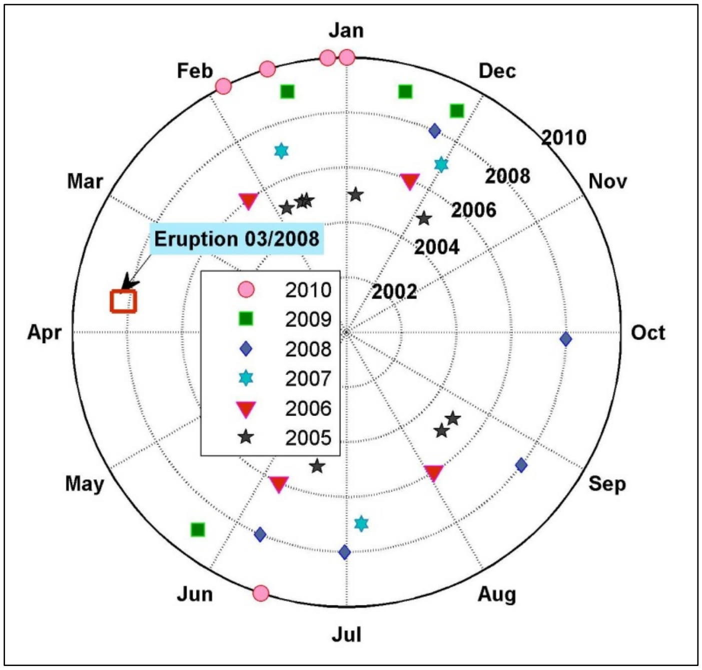

Figure B: Example of ATCOR-corrected HyspIRI-like spectra: Vegetation

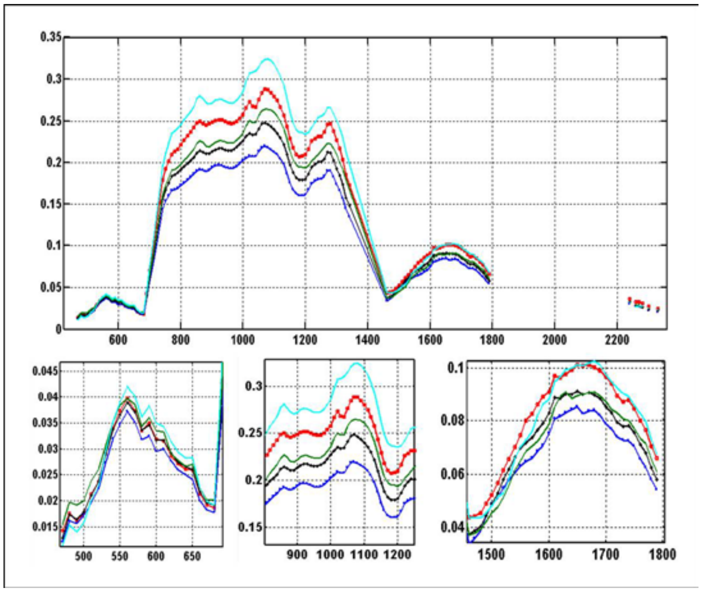

Figure C: Example of Cloud, Plume, and Shadow classification images developed in this project

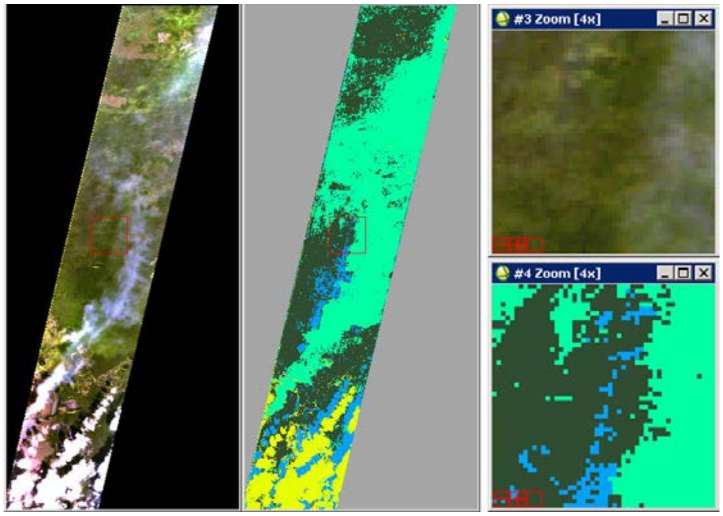

Figure D: Specific absorption coefficient spectra used by PROSPECT-5

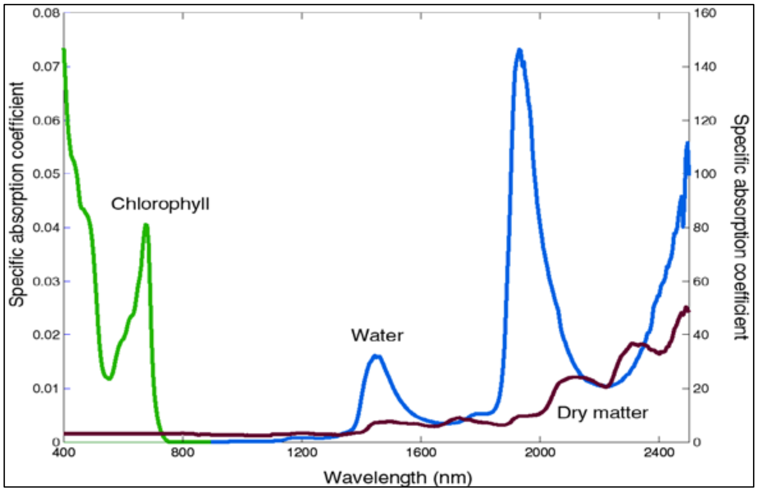

Figure E1: Effect of running PROSAILH at the laboratory (1-nm) and HyspIRI (10 nm) resolution on Chl-a,b retrieval

Chlorophyll a,b concentrations estimations by PROSAILH inversion with laboratory-like (left) and HyspIRI-like (right) absorption coefficient spectra τ(λ). Relative error ≅ 3%. Dark blue color represent pixels that were not processed due to clouds/shadows or no satellite data coverage or values close to zero.

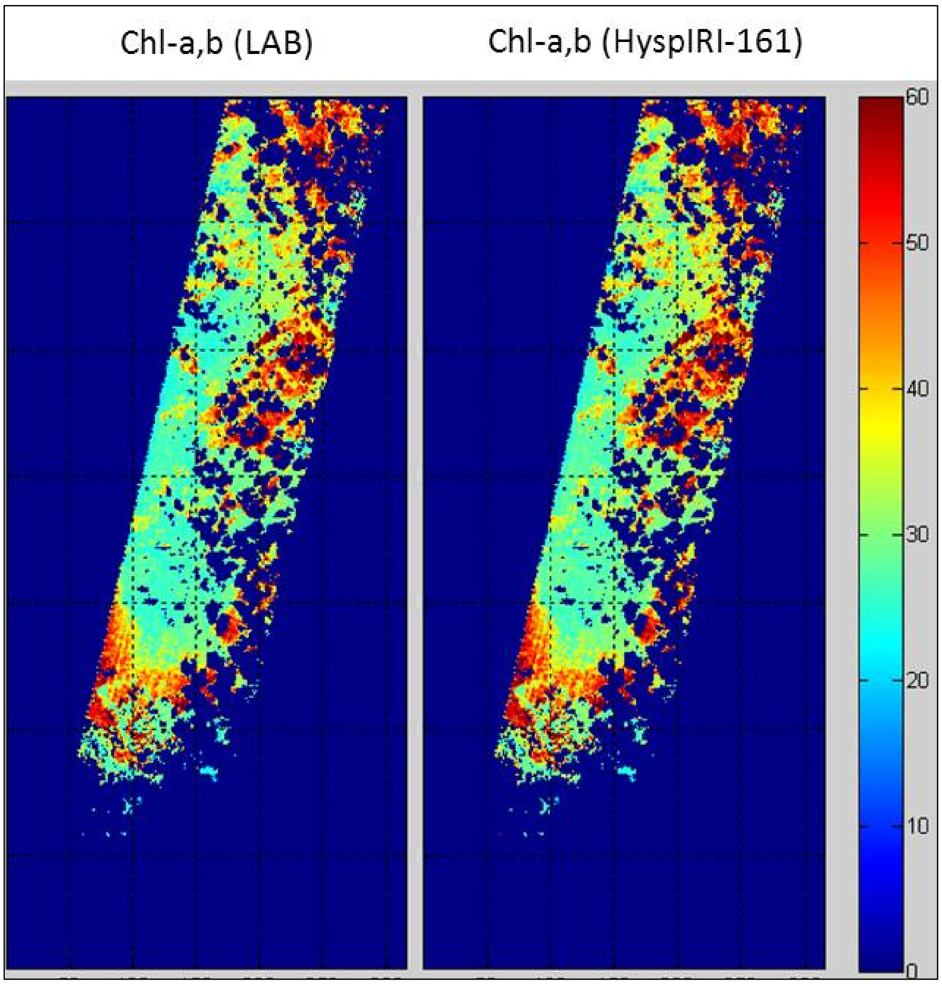

Figure E2: Effect of running PROSAILH at the sensor resolution, in case of MASTER data: observed vs. modeled spectra

Effect of running PROSAILH at the sensor resolution, in case of MASTER data over Belridge almond and pistachio orchards in San Joaquin Valley, CA (Cheng et al. 2013): observed vs. modeled spectra. Each line represents a median spectrum of 1000-5000 pixels in the MASTER image. Dashed lines labeled "modeled-M-#"" represent spectra that are modeled by PROSAILH that is run at the low resolution MASTER sensor resolution (see sect. 2.2.1). Spectra labeled "modeled-L-#" are obtained when PROSAILH generates spectra at high (laboratory) resolution of 1nm. Note the substantial differences in the approximation accuracy for the observed input spectra.

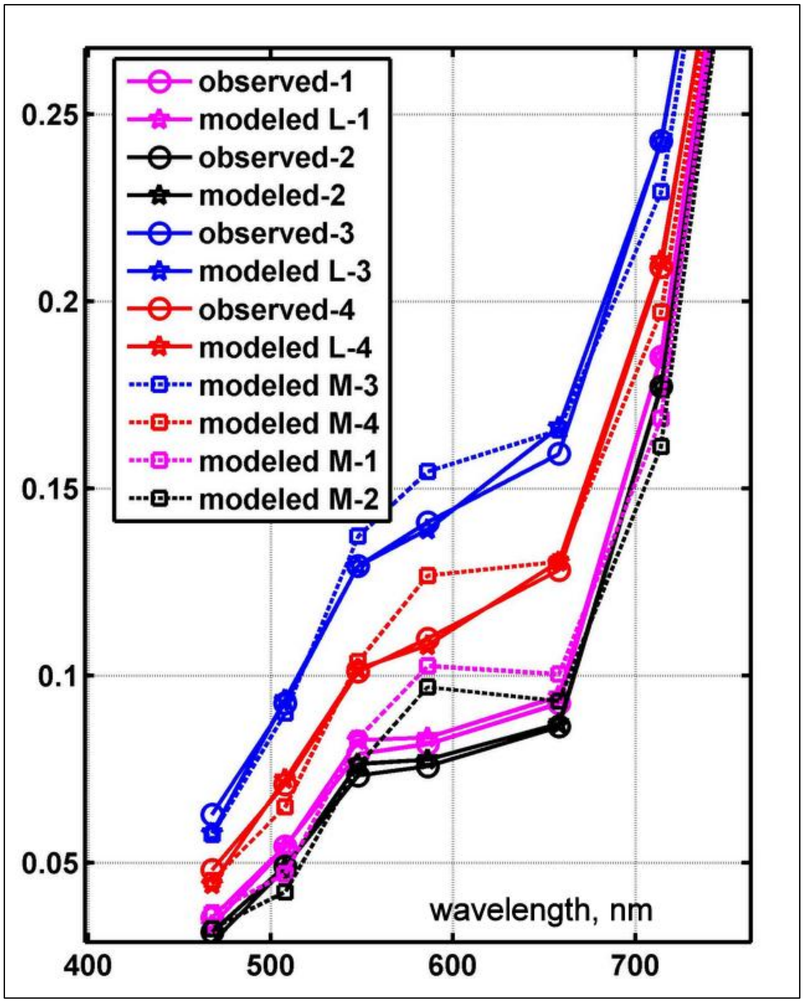

Figure E3: Effect of running PROSAILH at the sensor resolution, in case of MASTER data

Effect of running PROSAILH at the sensor resolution, in case of MASTER sensor. Note significant and non-uniform differences in the inversion results

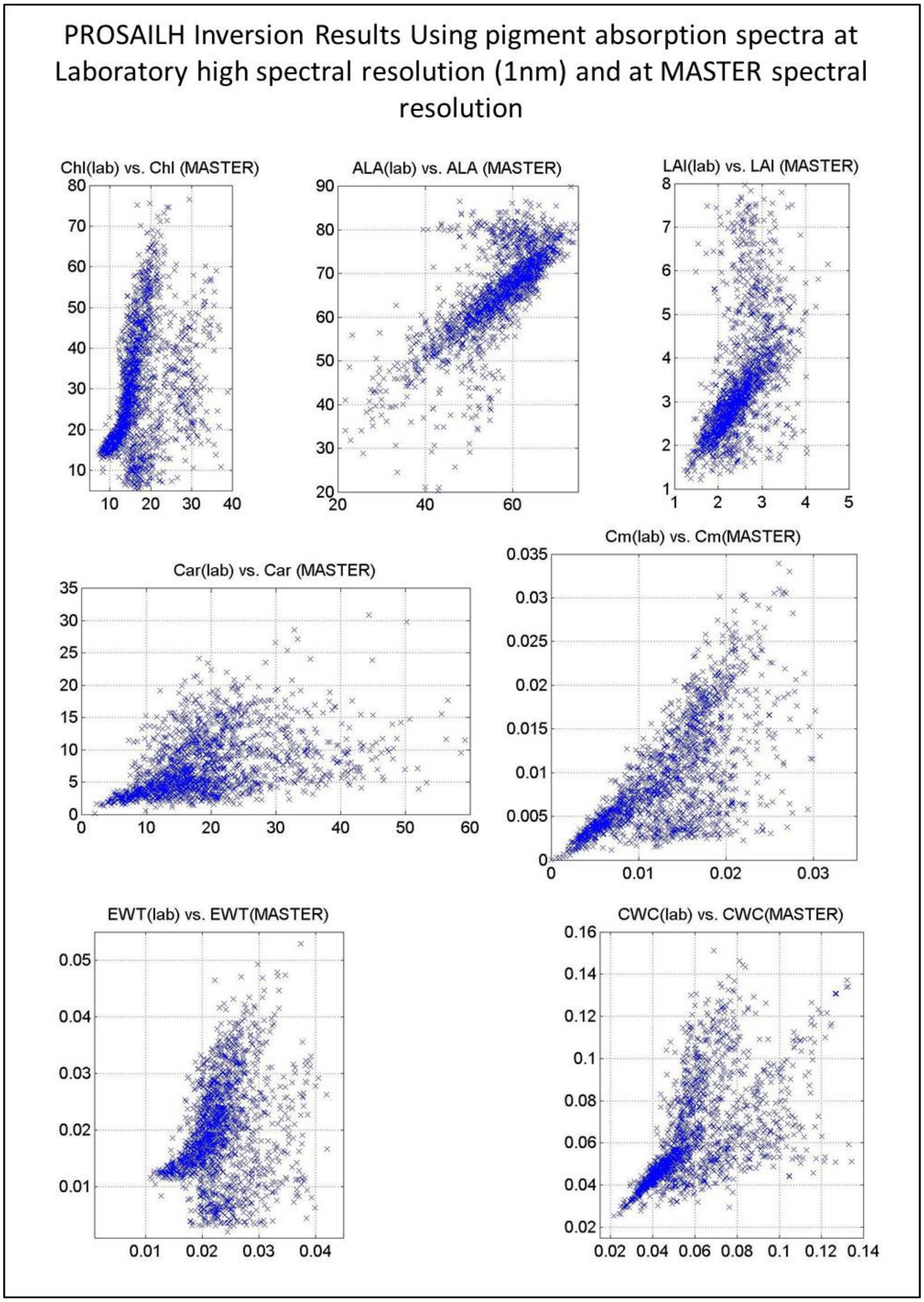

Figure F1: Soil spectra: the actually used one and the scaled ones

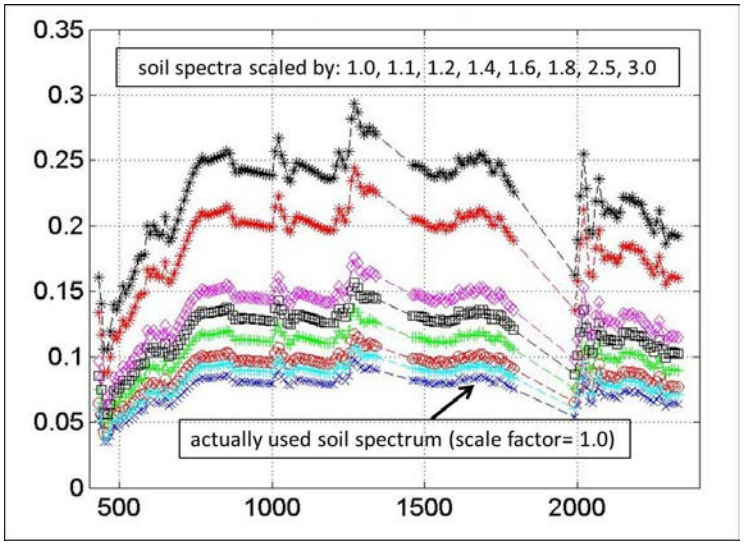

Figure F2: C_{brown} retrievals under different brightness of soil spectrum

Note the overall decrease in C_{brown} with brightening of the soil spectrum. Dark blue color represent pixels that were not processed due to clouds/shadows or no satellite data coverage or values close to zero.

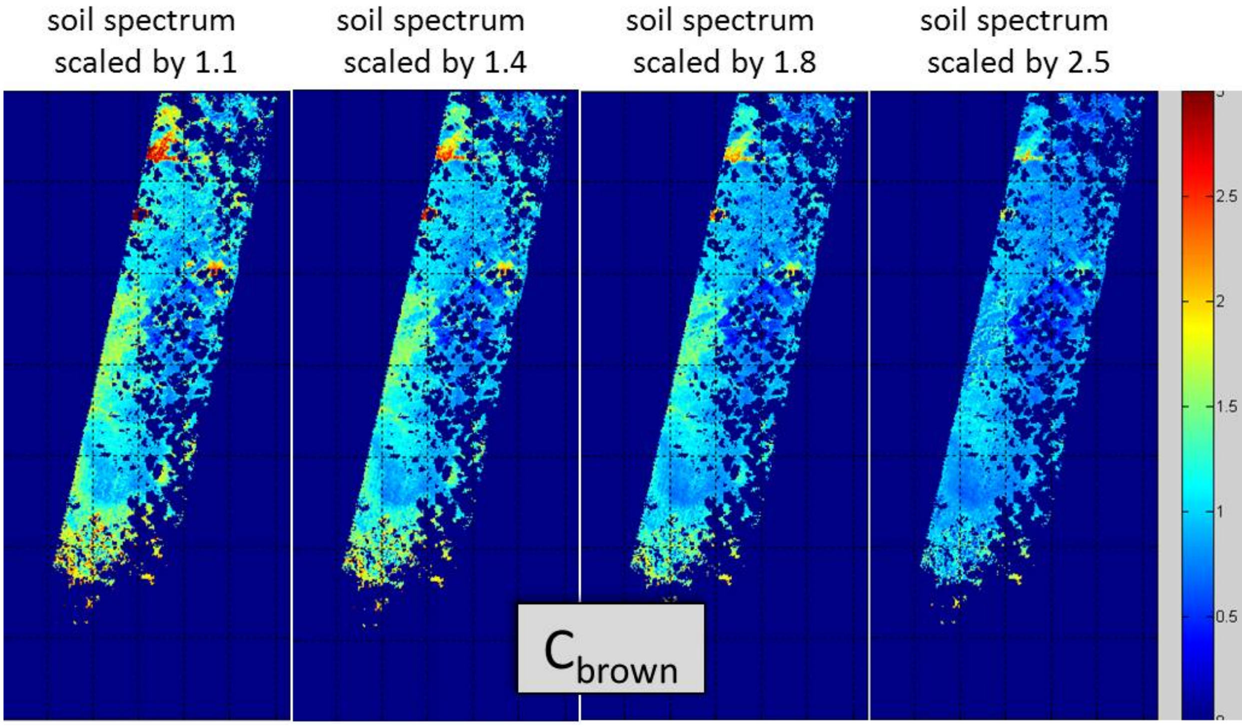

Figure G1: Brightness variability across images of the HyspIRI-161 sequence

Brightness variability across images of the HyspIRI-161 sequence before (left) and after relative normalization. Sun-view geometry of images dated 2005.01.17 and 2007.01.20 are very similar (see also Table 3 and Figure G3)

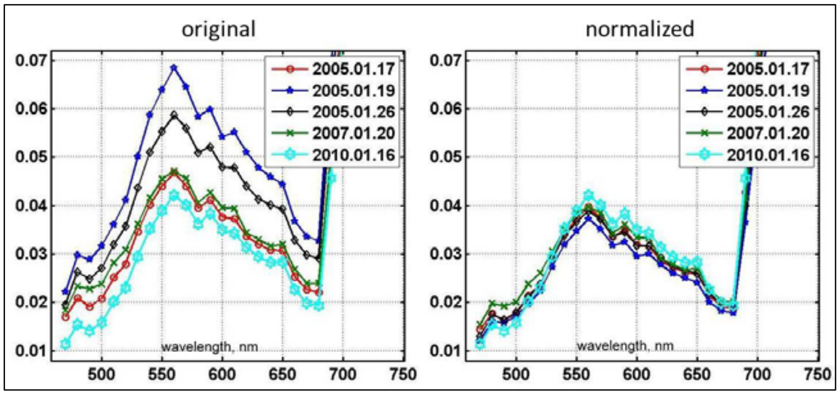

Figure G2: Instability of PROSAILH inversion for images with substantially varying sun-view geometry, in the example of Average Leaf Angle (ALA)

Instability of PROSAILH inversion for images with substantially varying sun-view geometry, in the example of Average Leaf Angle (ALA). Top row: inversion using non-normalized reflectance images. Bottom row: inversion using empirically normalized images. Note the short time intervals between first three dates. Dark blue color represent pixels that were not processed due to clouds/shadows or no satellite data coverage or values close to zero.

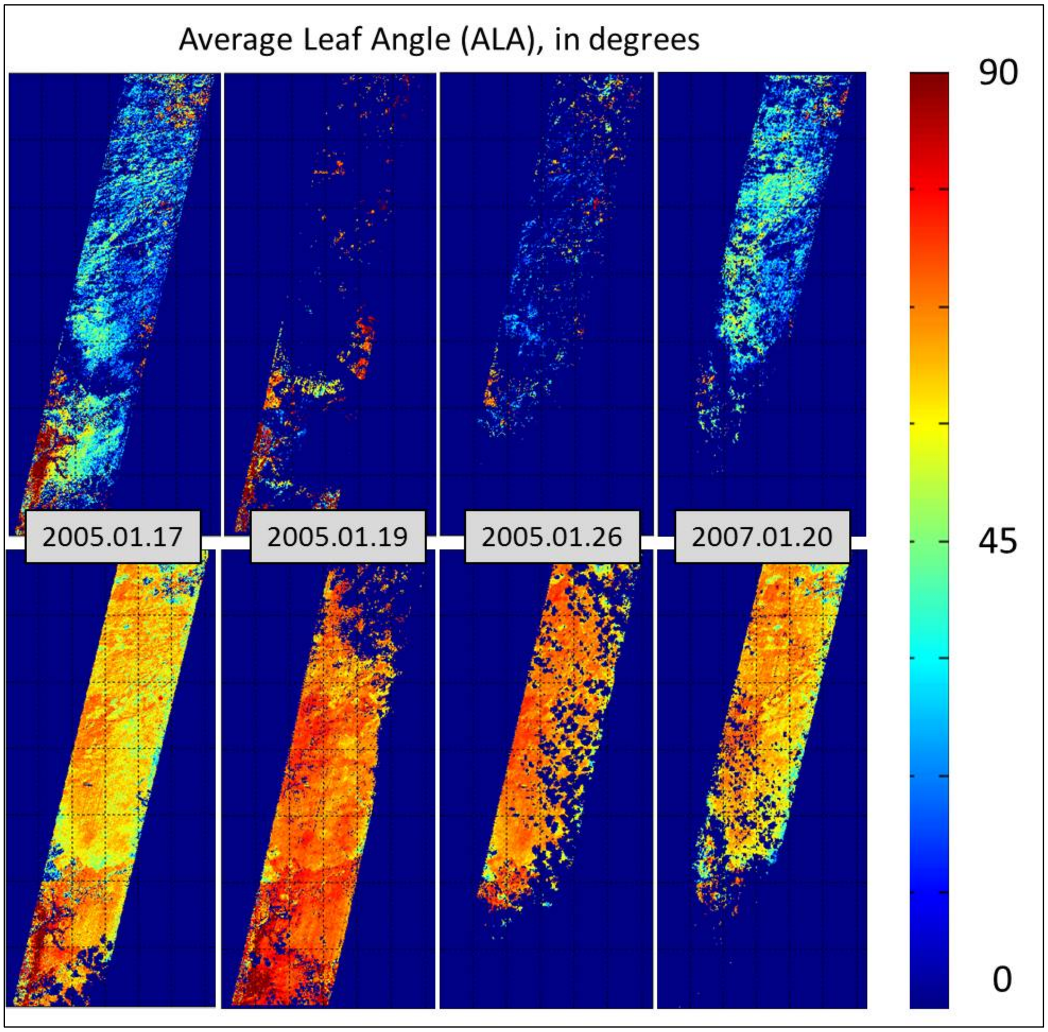

Figure G3: Sun-view geometries vs. empirical normalization coefficient β

Correspondence between sun-view geometries and statistically estimated relative normalization factor β (*cf.* Table 2). The colors representing the sun-view geometries is obtained by RGB-compositing sensor look, solar elevation, and relative solar azimuth angles. Note that similar sun-view geometries always have close values of β (the opposite statement does not hold, in general).

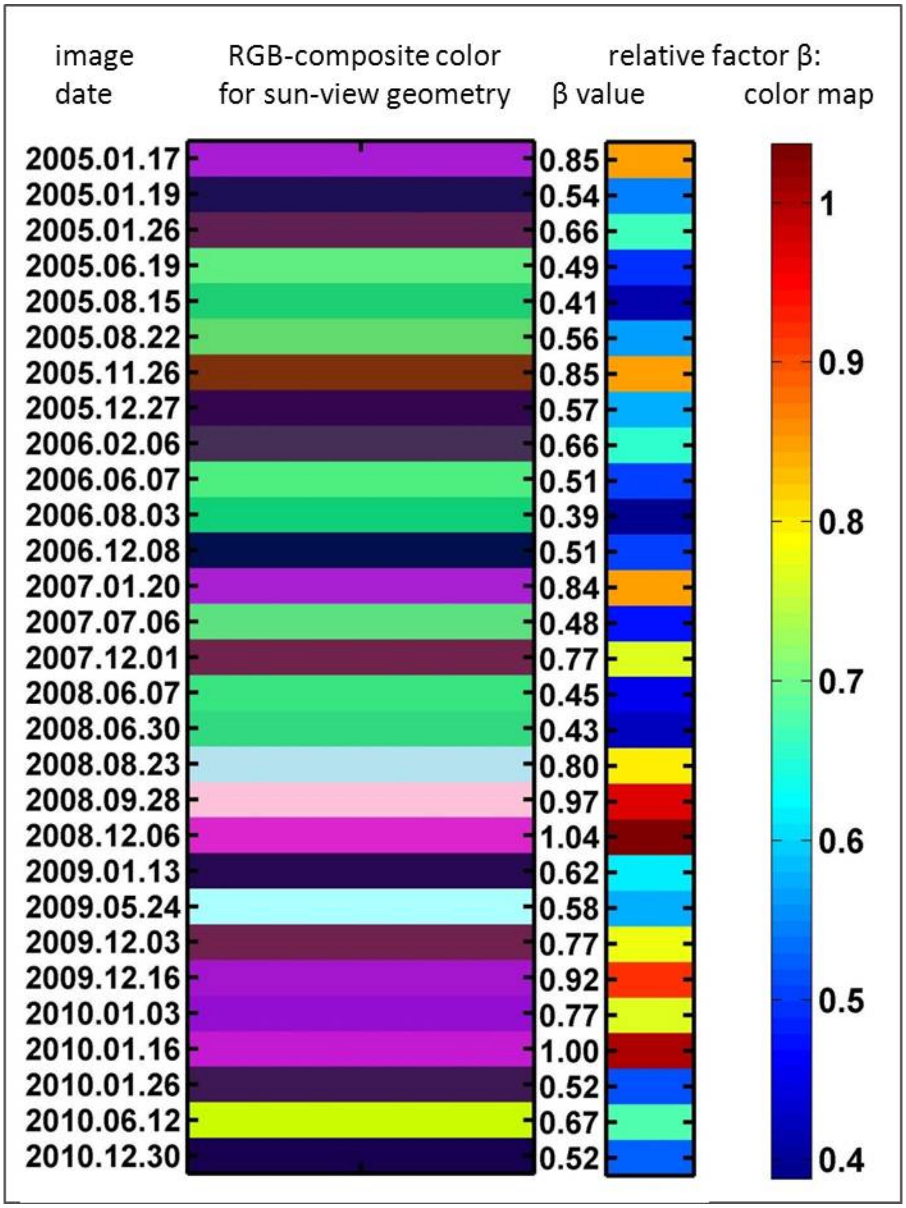

Figure H: ROIs

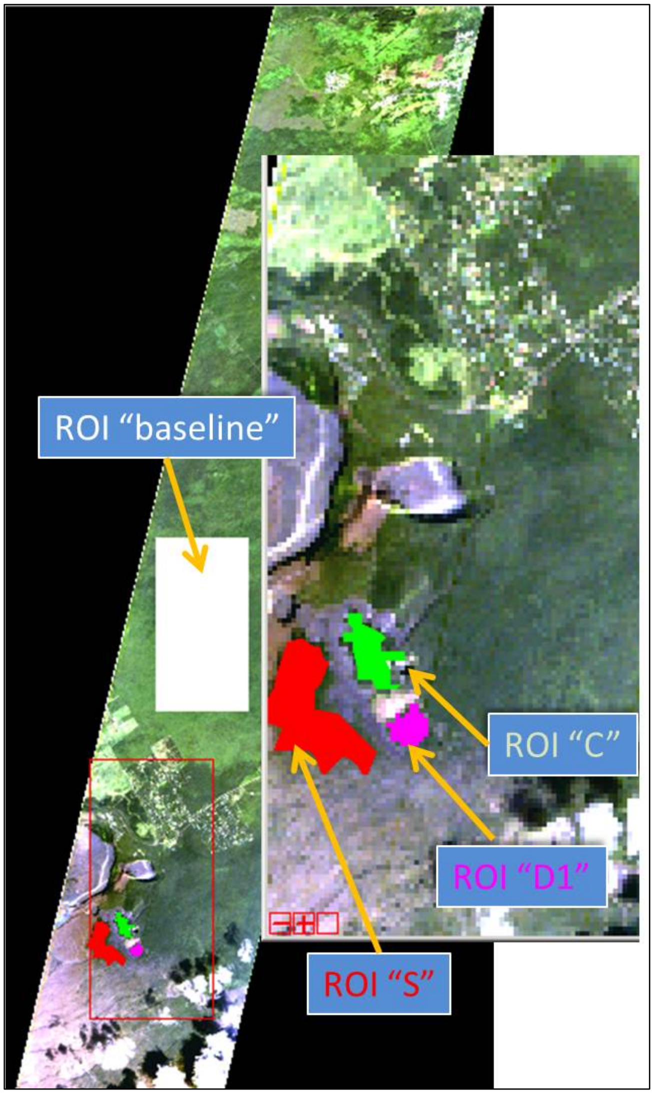

Figure J1: Leaves and Canopies of *Metrosideros Polymorpha* and *Myrica Faya*

Figure K1: LAI retrieval from PROSAILH for Metrosideros Polymorpha and Myrica Faya sites of Asner et al. 2006: note that the estimated LAI is generally higher for Myrica regions

Dark blue color represent pixels that were not processed due to clouds/shadows or no satellite data coverage or values close to zero.

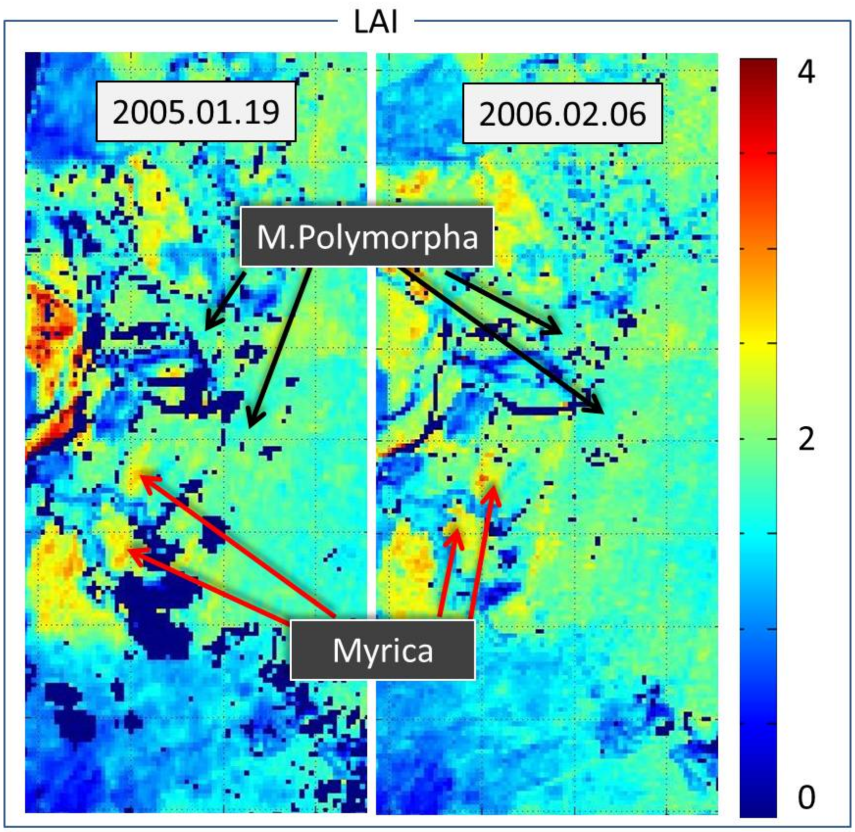

Figure K2: C_w retrieval from PROSAILH for Metrosideros Polymorpha and Myrica Faya sites of Asner et al. 2006: note that the estimated Cw is generally higher for Myrica regions .

Dark blue color represent pixels that were not processed due to clouds/shadows or no satellite data coverage or values close to zero.

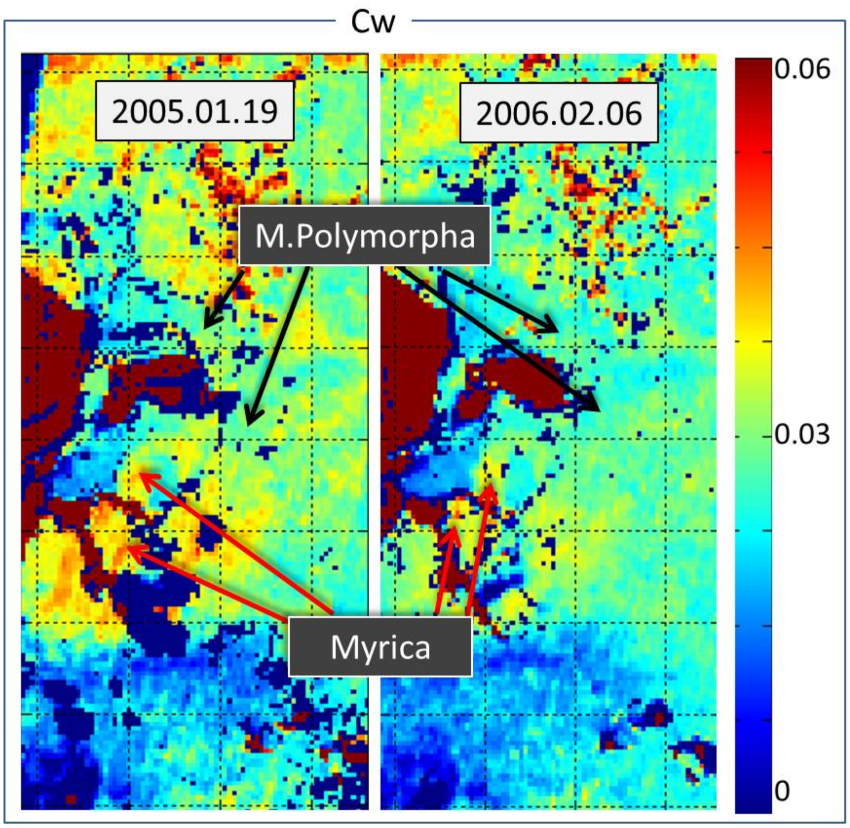

Figure L1: High-resolution images of ROIs (cf. Figure L2)

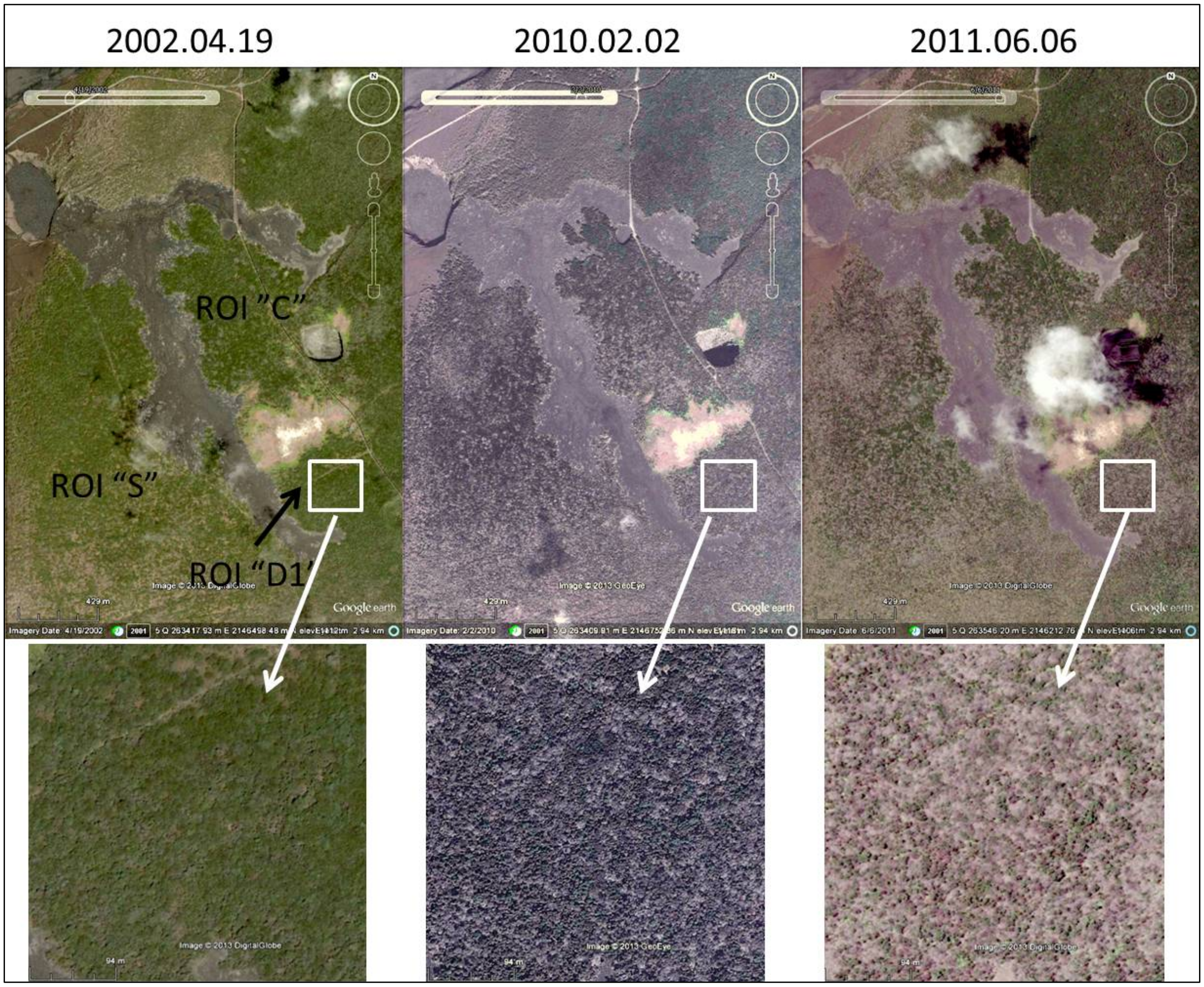

Figure L2: Zoomed image time series of the ratio to baseline ROI for selected vegetation properties during wet season before and after the eruption (note the apparent change in spatial pattern, consistent with vegetation degradation observable in Figure L1)

Dark blue color represent pixels that were not processed due to clouds/shadows or no satellite data coverage or values close to zero.

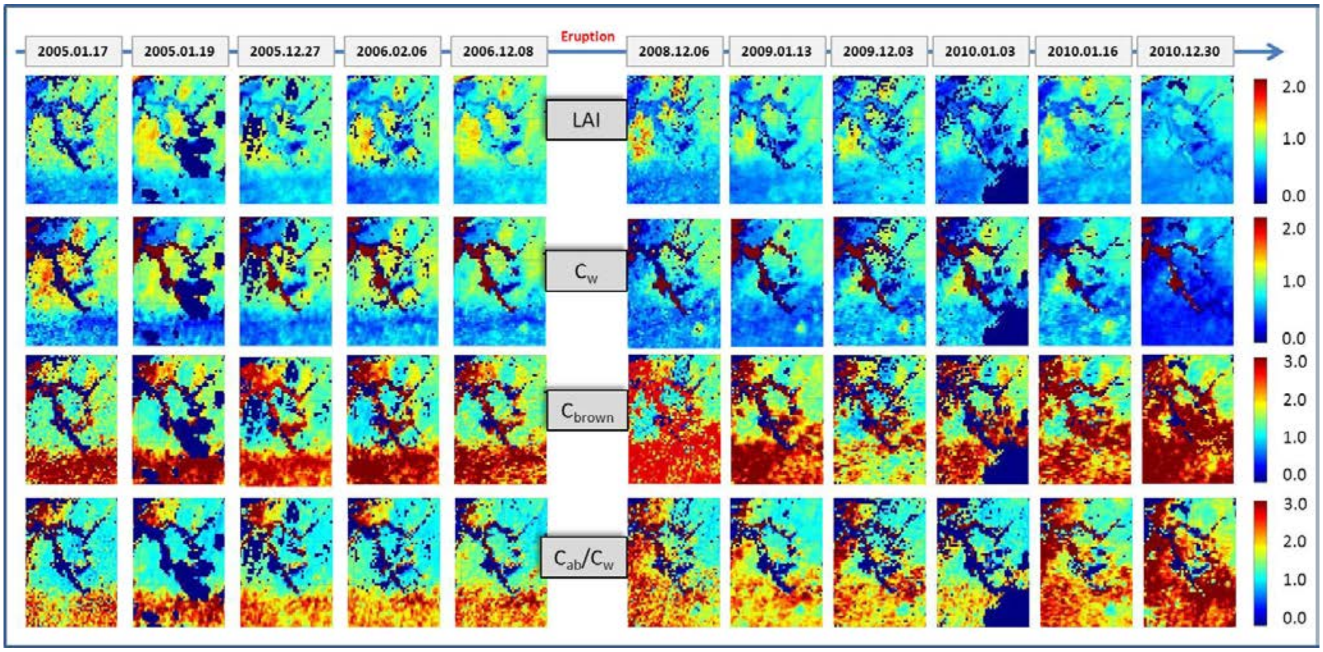

Figure MC: ROI “C” Mean Time series of PROSAILH parameters vs. Baseline ROI

ROI “C”: Mean time series of PROSAILH parameters retrieved from HyspIRI-161 images vs. the Baseline ROI. Wet season and dry season retrievals are colored in blue and red color, respectively. Red vertical line in each plot indicates the timing of Halemaumau vent opening (2008.03.19).

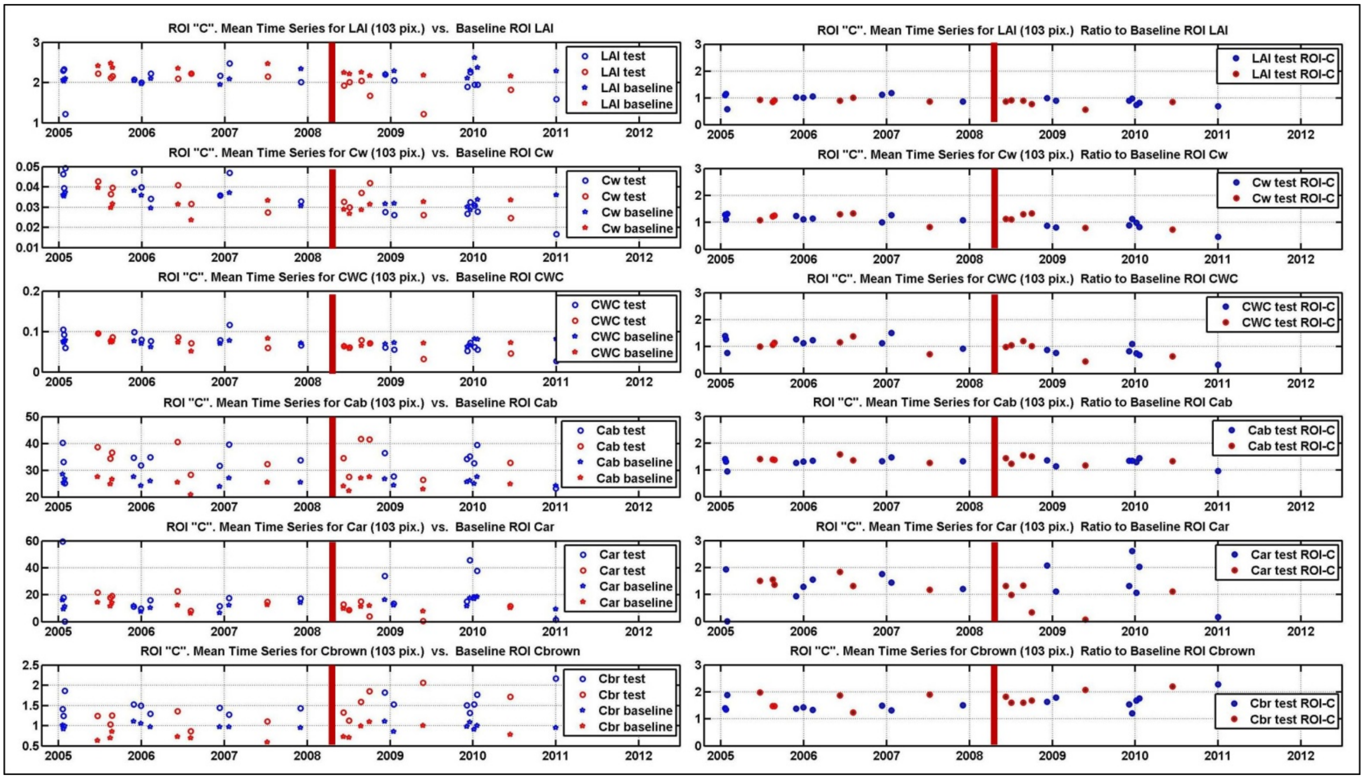

Figure MS: ROI “S” Mean Time series of PROSAILH parameters vs. Baseline ROI

ROI “S”: Mean time series of PROSAILH parameters retrieved from HyspIRI-161 images vs. the Baseline ROI. Wet season and dry season retrievals are colored in blue and red color, respectively. Red vertical line in each plot indicates the timing of Halemaumau vent opening (2008.03.19).

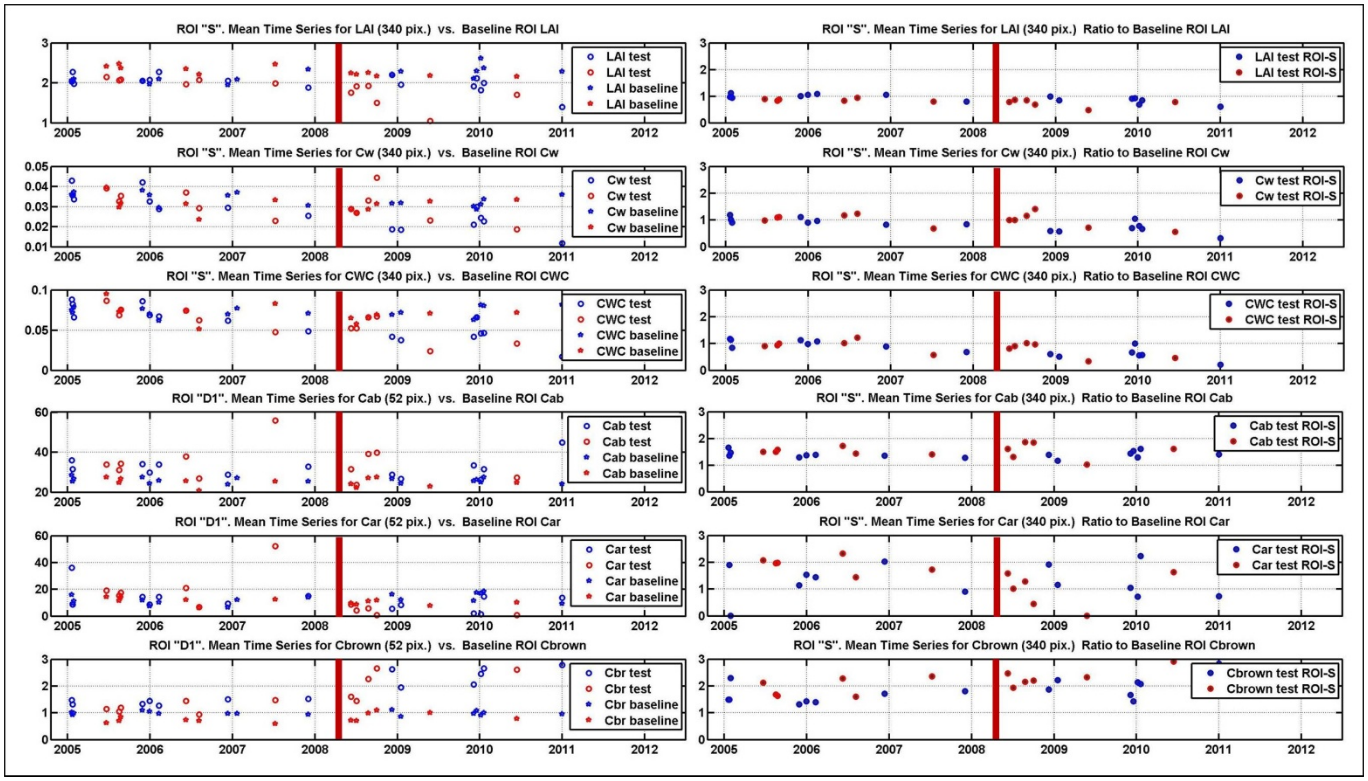

Figure MD1: ROI “D1” Mean Time series of PROSAILH parameters vs. Baseline ROI

ROI “D1”: Mean time series of PROSAILH parameters retrieved from HyspIRI-161 images vs. the Baseline ROI. Wet season and dry season retrievals are colored in blue and red color, respectively. Red vertical line in each plot indicates the timing of Halemaumau vent opening (2008.03.19).

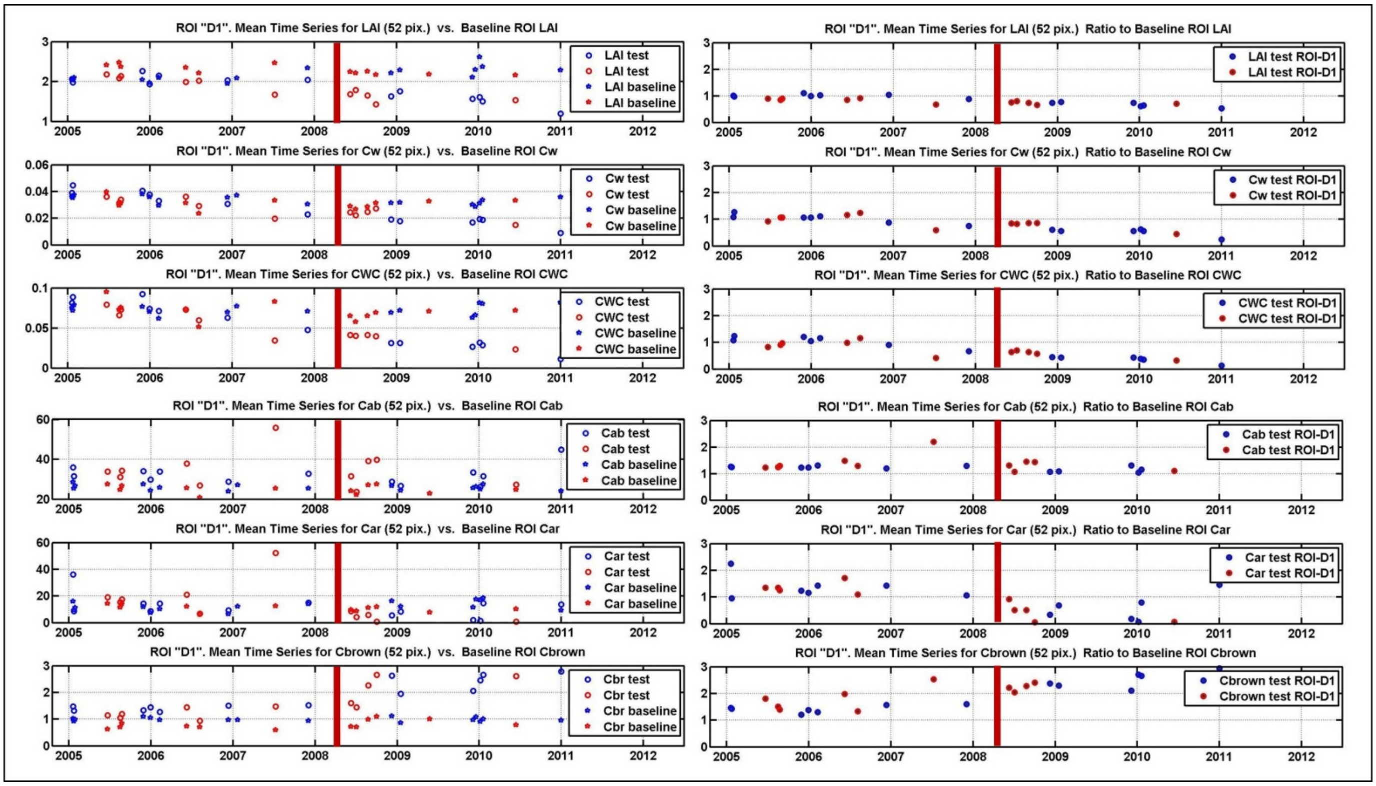

Table 1: PROSAILH parameter information

symbol/ acronym	name	units	initial value	range	assumed a known constant
N	leaf structure parameter	-	1.5	[1, 3]	no
C_{ab}	chlorophyll a+b content	$\mu g/cm^2$	30	[1e-8, 300]	no
Car	carotenoids content	$\mu g/ cm^2$	8	[1e-8, 200]	no
C_{brown}	brown pigments content	-	0.05	[1e-8, 3.0];	no
C_w	equivalent water thickness	cm or g/ cm^2	0.01	[1e-8, 0.30]	no
C_m	dry matter content	g/ cm^2	0.01	[1e-8, 0.40];	no
ALA	average leaf angle (elliptical LIDF)	degrees	50	[0.1, 89.9]	no
LAI	leaf area index	m^2/ m^2	1	[1e-8 - 15]	no
q	hot spot coefficient	-	0.5	[0.02-2.0]	no
SkyL	Ratio of diffused to total incident radiation	-	0.23	-	yes (*)
sza	Solar zenith angle	degrees	from image	-	yes (*)
vza	Viewing zenith angle	degrees	from image	-	yes (*)
raa	Relative azimuth angle	degrees	from image	-	yes (*)
ρ_s	Soil reflectance (Lambertian)	-	from image	-	yes
					(*) - after image normalization

Table 2: What happens with vegetation properties retrieved by PROSAILH when soil brightness increases

symbol	name	direction of change
Cab	chlorophyll a+b content	decrease
Car	carotenoids content	decrease
Cbrown	brown pigments content	decrease
Cw	equivalent water thickness	decrease
Cm	dry matter content	decrease
ALA	average leaf angle (elliptical LIDF)	increase
LAI	leaf area index	increase
CWC	canopy water content (EWT*LAI)	increase

Table 3: Hyperion Sun-View Geometry and Empirical Between-Date Normalization

Image #	Date	Sensor Look Angle	Sun Elevation Angle	Sun Azimuth	Sun Azimuth Relative to Sensor	Norm Factor, β
1	'2005.01.17'	7.7	41.5	143.9	113.1	0.8477
2	'2005.01.19'	-17.4	39.9	140.5	-63.5	0.5438
3	'2005.01.26'	-5.3	41.9	140.1	-63.1	0.6626
4	'2005.06.19'	-5.4	64.2	76.2	0.8	0.4947
5	'2005.08.15'	-17.3	61.0	96.4	-19.4	0.4116
6	'2005.08.22'	-5.1	62.1	102.2	-25.2	0.5629
7	'2005.11.26'	0.0	43.5	149.2	-162.2	0.8476
8	'2005.12.27'	-13.6	39.1	145.6	-68.6	0.5734
9	'2006.02.06'	-10.4	43.5	136.2	-59.2	0.6586
10	'2006.06.07'	-8.7	64.3	77.4	-0.4	0.5092
11	'2006.08.03'	-20.0	60.9	88.8	-11.8	0.3875
12	'2006.12.08'	-22.8	40.1	146.2	-69.2	0.5079
13	'2007.01.20'	7.9	41.7	143.1	113.9	0.844
14	'2007.07.06'	-6.2	62.9	78.1	-1.1	0.4771
15	'2007.12.01'	-2.2	42.2	148.2	-71.2	0.7703
16	'2008.06.07'	-12.5	63.3	77.5	-0.5	0.4511
17	'2008.06.30'	-13.6	62.0	76.9	0.1	0.4274
18	'2008.08.23'	9.8	63.0	103.8	153.2	0.803
19	'2008.09.28'	23.3	59.4	132.9	124.1	0.9699
20	'2008.12.06'	16.9	42.5	150.7	106.3	1.0367
21	'2009.01.13'	-15.5	39.2	141.4	-64.4	0.6163
22	'2009.05.24'	8.4	66.1	81.8	175.2	0.5769
23	'2009.12.03'	-2.5	41.9	148.3	-71.3	0.7737
24	'2009.12.16'	7.0	40.8	148.7	108.3	0.923
25	'2010.01.03'	3.8	39.9	145.8	111.2	0.7693
26	'2010.01.16'	12.8	41.3	144.1	112.9	1
27	'2010.01.26'	-11.6	41.0	138.7	-61.7	0.5163
28	'2010.06.12'	13.8	66.0	76.4	-179.4	0.6728
29	'2010.12.30'	-18.8	38.3	144.0	-67.0	0.5208

Table 4: Strength of evidence (in terms of two-sample t-test p-value) that the ratio to baseline ROI vegetation properties significantly decreased or increased after the Halemaumau eruption.

Two-sample t-test p-value (alternative hypothesis: "Ratio to Baseline DECREASED")			
	ROI "C"	ROI "S"	ROI "D1"
LAI	0.010141	0.000268	0.021371
Cw	0.451162	0.803092	0.440887
CWC	0.126032	0.257056	0.186301
Cab	0.760949	0.935836	0.969659
Car	0.027431	0.12341	0.669799
Cbrown	0.994519	0.998582	0.945563
Two-sample t-test p-value (alternative hypothesis: "Ratio to Baseline INCREASED")			
	ROI "C"	ROI "S"	ROI "D1"
LAI	0.989859	0.999732	0.978629
Cw	0.548838	0.196908	0.559113
CWC	0.873968	0.742944	0.813699
Cab	0.239051	0.064164	0.030341
Car	0.972569	0.87659	0.330201
Cbrown	0.005481	0.001418	0.054437
Strong Evidence			
Medium Evidence			
Weak Evidence			